



Published in final edited form as:

ACS Nano. 2014 May 27; 8(5): 4450–4464. doi:10.1021/nn5012754.

## Aspect Ratio Plays a Role in the Hazard Potential of CeO<sub>2</sub> Nanoparticles in Mouse Lung and Zebrafish Gastrointestinal Tract

Sijie Lin<sup>1,¶</sup>, Xiang Wang<sup>1,¶</sup>, Zhaoxia Ji<sup>1,¶</sup>, Chong Hyun Chang<sup>1</sup>, Yuan Dong<sup>2</sup>, Huan Meng<sup>1,3</sup>, Yu-Pei Liao<sup>3</sup>, Meiying Wang<sup>3</sup>, Tze-Bin Song<sup>4</sup>, Sirius Kohan<sup>5</sup>, Tian Xia<sup>1,3</sup>, Jeffrey I. Zink<sup>6</sup>, Shuo Lin<sup>2</sup>, and André E. Nel<sup>1,3,\*</sup>

<sup>1</sup>Center for Environmental Implications of Nanotechnology, California NanoSystems Institute, University of California, Los Angeles, California 90095, United States

<sup>2</sup>Department of Molecular, Cell and Developmental Biology, University of California, Los Angeles, California 90095, United States

<sup>3</sup>Division of NanoMedicine, Department of Medicine, University of California, Los Angeles, California 90095, United States

<sup>4</sup>Department of Materials Science and Engineering, University of California, Los Angeles, California 90095, United States

<sup>5</sup>Brain Research Institute, University of California, Los Angeles, California 90095, United States

<sup>6</sup>Department of Chemistry and Biochemistry, University of California, Los Angeles, California 90095, United States

### Abstract

We have previously demonstrated that there is a relationship between the aspect ratio (AR) of CeO<sub>2</sub> nanoparticles and *in vitro* hazard potential. CeO<sub>2</sub> nanorods with AR = 22 induced lysosomal damage and progressive effects on IL-1 $\beta$  production and cytotoxicity in the human myeloid cell line, THP-1. In order to determine whether this toxicological paradigm for long aspect ratio (LAR) CeO<sub>2</sub> is also relevant *in vivo*, we performed comparative studies in the mouse lung and gastrointestinal tract (GIT) of zebrafish larvae. Although oropharyngeal aspiration could induce acute lung inflammation for CeO<sub>2</sub> nanospheres and nanorods, only the nanorods with the highest AR (C5) induced significant IL-1 $\beta$  and TGF- $\beta$ 1 production in the bronchoalveolar lavage fluid (BALF) at 21 days but not inducing pulmonary fibrosis. However, after a longer duration (44 days) exposure to 4 mg/kg of the C5 nanorods, more collagen production was seen with CeO<sub>2</sub>

\*Corresponding Author: Andre Nel, M.D., Department of Medicine, Division of NanoMedicine, UCLA School of Medicine, 52-175 CHS, 10833 Le Conte Ave, Los Angeles, CA 90095-1680. Tel: (310) 825-6620, Fax: (310) 206-8107, anel@mednet.ucla.edu.

¶Contribute equally

Supporting Information Available

Additional figures on the IL-1 $\beta$  production by THP1 and bone marrow derived macrophages (BMDM) after exposure to CeO<sub>2</sub> nanoparticles, H&E stained lung section from mice exposed to CeO<sub>2</sub> for 40 h, Masson's Trichrome stained lung section from mice exposed to CeO<sub>2</sub> for 21 days, representative microscopic images of zebrafish larvae in control and CeO<sub>2</sub> exposed groups, representative TEM images of the pseudo-feces containing CeO<sub>2</sub> nanospheres (C1) and nanorods (C5), and representative TEM images showing the interaction of C5 with microvilli in the gastrointestinal tract of zebrafish larvae. This material is available free of charge *via* the Internet at <http://pubs.acs.org>.

nanorods vs. nanospheres after correcting for Ce lung burden. Using an oral-exposure model in zebrafish larvae, we demonstrated that C5 nanorods also induced significant growth inhibition, a decrease in body weight, and delayed vertebral calcification. In contrast, CeO<sub>2</sub> nanospheres and shorter nanorods had no effect. Histological and transmission electron microscopy (TEM) analyses showed that the key injury mechanism of C5 was in the epithelial lining of the GIT, which demonstrated blunted microvilli and compromised digestive function. All considered, these data demonstrate that, similar to cellular studies, LAR CeO<sub>2</sub> nanorods exhibit more toxicity in the lung and GIT, which could be relevant to inhalation and environmental hazard potential.

## Keywords

CeO<sub>2</sub> nanoparticle; long aspect ratio; hazard potential; mouse lung; zebrafish gastrointestinal tract

Long aspect ratio (LAR) nanomaterials are increasingly being used in semiconductors, catalysts, microelectromechanical systems, food packaging and biomedicine because of the acquisition of unique physicochemical properties.<sup>1-5</sup> Because increased industrial use also raises the chances of human and environmental exposure, we have recently constructed a CeO<sub>2</sub> nanoparticle library in which the AR of the nanoparticles ranged from 1 (nanospheres) to >100 (nanorods).<sup>6</sup> CeO<sub>2</sub> is important because of its widespread use in fuel additives, polishing materials, energy production and biomedical applications.<sup>7-8</sup> In addition, more attention is paid to one-dimensional CeO<sub>2</sub> nanostructures like nanorods, nanowires, and nanotubes due to their high redox and catalytic activities. In a recent study, synthesis of CeO<sub>2</sub> nanoparticles with various shapes (nanopolyhedra, nanorods, and nanocubes) has demonstrated that nanorods exhibited the highest oxygen-storage capacity.<sup>9</sup> In another study, Zhou *et al.* showed the superior reduction capabilities of CeO<sub>2</sub> nanotubes compared to the conventional nanoparticles.<sup>10</sup> Using a human myeloid cell line, THP-1, we showed that CeO<sub>2</sub> nanorods with an AR = 22 can induce a progressive increase in IL-1 $\beta$  production by generating lysosomal damage and assembly of the NLRP3 inflammasome.<sup>6</sup> By contrast, CeO<sub>2</sub> nanospheres and shorter nanorods did not show any significant toxicity. A key question therefore becomes whether the AR of CeO<sub>2</sub> could also impact this material's *in vivo* hazard potential. An important target organ is the lung, because of the dispersive nature of these materials, including a recent demonstration that CeO<sub>2</sub> nanoparticles exhibit the potential to induce pulmonary fibrosis.<sup>7, 11</sup> Moreover, it is also important to consider the environmental impact of LAR materials, towards which we use zebrafish embryos and larvae as a model for studying the toxicity of oxide nanoparticles.<sup>12-14</sup>

The rodent lung is frequently used to assess the hazard potential of respirable engineered nanomaterials (ENM), including LAR materials such as TiO<sub>2</sub> nanobelts, single-wall (SWCNT) and multi-wall carbon nanotubes (MWCNTs).<sup>15-19</sup> Collectively, these studies show that LAR materials are capable of inducing acute neutrophilic as well as subchronic granulomatous inflammation, leading to pulmonary fibrosis.<sup>18-20</sup> One of the mechanisms by which LAR materials induce subchronic lung injury is triggering of frustrated phagocytosis in macrophages, which may fail to digest bio-persistent fibers more than 15  $\mu$ m in length.<sup>21</sup> At this length scale, materials such as asbestos fibers are capable of piercing the surface membrane of the phagocyte, leading to leakage of highly inflammatory hydrolytic enzymes

and reactive oxygen species (ROS), which result in chronic lung injury and fibrosis.<sup>21–23</sup> However, most CeO<sub>2</sub> nanorods do not fall into the fiber length scale, and it is important to consider other injury mechanisms in pulmonary macrophages, including lysosomal injury by LAR materials in the nm to the lower micron length scale.<sup>6, 18, 24–26</sup> Lysosomal injury results in the assembly of the NLRP3 inflammasome, which leads to IL-1 $\beta$  release by pulmonary macrophages; this cytokine may then initiate a progressive cascade that culminates in pulmonary fibrosis.<sup>18, 24–26</sup> The particle dose, subcellular localization and rate of clearance of the LAR materials from the lung establishes lung burden that, during CeO<sub>2</sub> nanoparticle overload, could determine whether an exposure will result in chronic injury.<sup>20–21, 23</sup> To date there has been no systematic dissection of the role of CeO<sub>2</sub> AR and shape in the events that may contribute to chronic or subchronic lung injury.

Although limited environmental studies showed that CeO<sub>2</sub> nanoparticles induce toxic effects in green algae and cyanobacteria,<sup>27–28</sup> no systematic toxicological analysis have been undertaken to assess the role of AR in environmental organisms. While it has been demonstrated that a LAR material such as CNTs can exert hazardous effects in daphnia, zebrafish and rainbow trout, these outcomes have been attributed to the hydrophobicity, state of agglomeration and heavy metal content rather than AR.<sup>29–32</sup> Interestingly, while SWCNTs can induce severe respiratory toxicity in fish due to gill damage<sup>31</sup>, it has been demonstrated that dendritic nickel nanoparticles can cause injury due to a shape effect in the gastrointestinal tract (GIT) of zebrafish larvae.<sup>33</sup> This injury, as a result of interference in epithelial folding and thinning of intestinal wall, was only observed during exposure to dendritic particles, but was not seen with spheres or nickel ions. Moreover, Gilbert *et al.* have recently shown that daphnia ingesting Ag nanowires display a distinct pattern of gene expression compared to the ones exposed to ionic Ag.<sup>34</sup> These results suggest that nanoparticle shape could play a role in GIT toxicity.

The objective of this study was to perform a comparative analysis of the effects of spherical and rod-shaped CeO<sub>2</sub> nanoparticles in the mouse lung and the GIT of zebrafish larvae. After the synthesis and characterization of a fresh library of CeO<sub>2</sub> nanospheres and nanorods, the biological impact of AR was confirmed in bone marrow macrophages before embarking on *in vivo* studies. Oropharyngeal aspiration of nanospheres and nanorods were performed in C57BL/6 mice to compare their ability to generate acute and subchronic inflammation in the lung. While all the CeO<sub>2</sub> nanoparticles could induce acute neutrophil inflammation in the lung, there was no significant correlation to AR, except that the longest nanorods (C5) could induce more IL-1 $\beta$  production than other materials. While all the materials could induce pulmonary fibrosis after 44 days, the longest rod (C5) induced more collagen deposition after correcting for lung burden. Oral exposure of zebrafish larvae to C5 nanorods also induced significant damage to the microvilli of the GIT epithelial cells. This led to digestive malfunction, which interfered in the growth and development of exposed larvae. These results are important in considering the potential toxicity of CeO<sub>2</sub> in occupational and environmental exposures.

## RESULTS

### Establishing a CeO<sub>2</sub> Aspect Ratio Library with Differential Toxicological Effects

Using hydrothermal synthesis, we prepared a library of CeO<sub>2</sub> nanoparticles that included nanospheres (AR=1, C1) and nanorods showing ARs of 8 (C2), 22 (C3), 52 (C4) and > 100 (C5) (Figure 1). The size, shape and AR of CeO<sub>2</sub> were characterized in their dry state using transmission electron microscopy (TEM), while the hydrodynamic diameter and surface charge were measured in deionized water, tissue culture medium (DMEM supplemented with 10 % FBS) and zebrafish growth medium (Holtfreter's buffer, supplemented with 100 ug/mL alginate). Figure 1 shows the representative TEM images of C1-C5. As shown in the included table, the average diameters of the nanorods were 7~10 nm, while the average lengths ranged from 50 nm to >1 μm. When dispersed in the tissue culture and Holtfreter's media, the hydrodynamic diameters of the CeO<sub>2</sub> nanoparticles ranged from 200 nm to 1.5 μm. It should be noted that the hydrodynamic diameters reported here for the CeO<sub>2</sub> nanorods only represent "relative" size and cannot be used to infer exact particle size. Nonetheless, our studies on CNTs demonstrate the utility of the DLS measurement as a qualitative index of the state of dispersal of long aspect ratio materials.<sup>6, 25-26</sup> While the zeta potential of the CeO<sub>2</sub> nanoparticles were in the range of 10 to 40 mV in distilled water, the surface charge became negative (-10 to -30 mV) upon coating with FBS or alginate.

In order to confirm the biological impact of AR variation, we used the myeloid cell line, THP-1, and bone marrow derived macrophages (BMDM) to determine whether the nanospheres and nanorods differ in their ability to initiate IL-1β production. We have previously shown that IL-1β release from myeloid cells and macrophages is determined by the impact of AR on the lysosome.<sup>25-26</sup> As shown in Figure S1A and B, cellular incubation with CeO<sub>2</sub> nanospheres and nanorods resulted in a progressive increase in IL-1β production in accordance with the AR. The effects of the CeO<sub>2</sub> nanorods became statistically significant above AR of 22. We confirmed that this effect involves lysosome activation and NLRP3 inflammasome assembly (not shown).<sup>6</sup>

### Acute Pulmonary Exposure to CeO<sub>2</sub> Nanospheres and Nanorods

C57BL/6 mice were used for exposure to 0.5, 1, 2, and 4 mg/kg of the C5 nanorods by oropharyngeal aspiration. The mice were sacrificed after 40 hr to collect bronchoalveolar lavage fluid (BALF) and lung tissue. Aspiration of Min-U-Sil (quartz or QTZ) was used as positive control. Examination of the BALF showed a dose-dependent increase in the neutrophil cell count, along with an increase in LIX (LPS-induced CXC chemokine), which is involved in neutrophil chemotaxis (Figure 2A, B). We also observed an increase in IL-1β production, which may comprise the early phase of a delayed injury response for some LAR materials (Figure 2C).<sup>24-26</sup> QTZ also induced increased IL-1β production. Based on the dose response data for C5 nanorods, we selected 2 mg/kg for comparative analysis of C1, C2, C3 and C5 in further lung exposure studies.

In a comparative study in which animal sacrifice was performed after 40 hr, all the nanoparticles could induce an increase in neutrophil cell counts, with a tendency for the acute inflammatory response to be higher for the LAR materials. The neutrophil cell counts

for C5 ( $3.2 \pm 0.7 \times 10^4/\text{mL}$ ) was significantly higher than for C1 ( $2.0 \pm 0.5 \times 10^4/\text{mL}$ ) (Figure 3A). However, this effect was accompanied by a non-selective but statistically significant increase in LIX levels for all particles tested (Figure 3B). The trend towards more inflammation by C5 was confirmed by H&E staining, which showed visual evidence of more acute inflammatory infiltrates around small- and medium-sized airways in lung of animals receiving the LAR particles (Figure S2). Again, the effect of the C5 nanorods was most pronounced (Figure S2). QTZ also induced significant increases in neutrophil counts and LIX levels in the BALF along with inflammatory changes in the lung (Figure 3A, B, and Figure S2). In contrast, the data for IL-1 $\beta$  production was quite different in that only C5 and QTZ induced significant increases in the BALF (Figure 3C). This suggested to us that, similar to the C5 dose response study, it would be important to address possible delayed injury.

### C5 Nanorods Show an Exaggerated Pro-Fibrogenic Response after Subchronic Exposure

In order to determine whether the observed IL-1 $\beta$  production at 40 hr is indicative of subchronic lung injury, we performed a study in which the animal sacrifice was performed 21 days after oropharyngeal instillation of C1, C3 and C5 at 2 mg/Kg. No evidence of neutrophil infiltration was obtained at this point (data not shown). While IL-1 $\beta$  levels also returned to baseline (not shown), measurement of TGF- $\beta$ 1 levels in the BALF showed that C5 induced a significant increase in TGF- $\beta$ 1 production, while C1 and C3 failed to induce a response (Figure 4A). However, none of the materials induced collagen deposition, as determined by a Sircol assay (Figure 4B) or Masson's trichrome staining of the lung sections (Figure S3). In contrast, QTZ induced a significant TGF- $\beta$ 1 production and collagen deposition (Figure 4A, B and S3). Because collagen deposition by TiO $_2$  nanobelts was seen to occur after several months,<sup>19</sup> a third series of experiments were undertaken in which sacrifice was performed 44 days after oropharyngeal aspiration of 4 mg/Kg. In this scenario, clear evidence was obtained of increased TGF- $\beta$ 1 production in the BALF (Figure 5A), along with increased collagen content in lung tissue (Figure 5B) and positive (blue color) trichrome staining (Figure 5C) for all tested materials, including QTZ. However, since ENMs with different ARs may have different rates of retention and bioavailability, we used inductively coupled plasma optical emission spectrometry (ICP-OES) to determine the total lung burden for Ce in C1 and C5 exposed animals. This demonstrated that there was indeed a significant difference in the lung burden of nanospheres and nanorods (Figure 5D). That is, the total Ce content in the lung of C1 exposed animals was six times higher than C5, suggesting a higher clearance rate and/or lower bioavailability for C5 comparison to C1. Use of the Ce content to adjust the collagen content in the lung (*i.e.*, expressing collagen content per unit mass of Ce), demonstrated that there was indeed more collagen deposition per unit dose of C5 (Figure 5E). These data indicate that while all CeO $_2$  nanoparticles induce pulmonary fibrosis at a dose of 4 mg/Kg, the response is strongest for C5, showing that AR could play a role in subchronic lung injury.

### AR Plays a Role in Growth Inhibition and Development of Zebrafish Larvae

We developed a pulse-exposure method for zebrafish larvae in petri dishes to limit the amount of CeO $_2$  nanoparticles that would be required for exposures in standard aquarium tanks. Petri dish exposure also limits the amount of hazardous waste being generated. The

exposure sequence is summarized in Figure 6A and discussed in detail in the Experimental Section. Briefly, groups of 30 larvae 5 days post-fertilization (dpf) were incubated with 25  $\mu\text{g}/\text{mL}$  C1, C3, C4 and C5 nanoparticles in each petri dish for 6 hr. The larvae were carefully and thoroughly washed before returning them to 3L aquarium tanks for regular maintenance. Second and third round pulse-exposures were carried out on the same larvae at 8 and 11 dpf, respectively. Twenty nm citrate-coated silver nanoparticles (AgNPs) were used as a positive control.<sup>35–37</sup> The larvae were assessed for overall health status, survival rate, gross morphological abnormalities, body length, weight, and number of calcified vertebrae (as a biomarker of skeletal development). While no significant mortality was observed for any of the  $\text{CeO}_2$  nanomaterials (Figure 6B), the larval length was significantly reduced by C4 and C5 exposures at 14 dpf compared to larvae exposed to C1 and C3 (Figure S4). While the larval morphology was grossly normal, the absence of dorsal and anal fin structures in the C4 and C5-exposed larvae suggested delayed development. In contrast, the larvae exposed to AgNPs showed a decreased survival rate, smaller size, and higher rate of morphological abnormalities (*e.g.*, the bent spine depicted in Figure S4). Quantitative expression of the measurements of larval length and weight also confirmed that C5-exposed animals had significant growth retardation compared to the control or C1/C3-exposed animals (Figure 6C and D). The same was true for AgNPs exposure. Since calcification of skeletal structures occurs in a caudal-to-rostral fashion, vertebral calcification is also a good parameter to assess larval development.<sup>38</sup> Calcification can be assessed by the green fluorescent chromophore, calcein, which is taken up and allows visualization of the calcified vertebrae. Quantification of the number of calcified vertebrae showed that larvae exposed to C5 (and AgNPs) had significantly fewer calcified vertebral segments by 14 dpf (Figure 6E). Taken together, both qualitative and quantitative assays demonstrate an AR threshold, above which  $\text{CeO}_2$  nanorods induce growth inhibition and abnormal development. This raises the question of the site(s) of injury by LAR materials in larvae.

### Assessment of $\text{CeO}_2$ Nanoparticle Uptake in the GIT of Zebrafish Larvae

In order to study  $\text{CeO}_2$  bioavailability, leading to interference in larval growth and development, we initially used light optical microscopy to look for the presence of the nanoparticles in the zebrafish larvae. This demonstrated the presence of  $\text{CeO}_2$  aggregates in the GIT lumen of larvae at 120 hpf (Figure 7A, left panel). The presence of  $\text{CeO}_2$  was confirmed by a signature  $\text{CeO}_2$  Raman peak, using confocal Raman microscopy (Figure 7A, right panel).<sup>39–40</sup> Raman spectra collected from the skin, fins or blood vessels did not show the presence of  $\text{CeO}_2$ , suggesting the GIT is a major target organ. This notion was strengthened by the lack of any  $\text{CeO}_2$  uptake in the GIT of 72 hpf embryos, which lacks a mouth opening for feeding (not shown). In contrast, 120 hpf larvae do express a mouth opening (Figure 7B).

Further studies were carried out to assess the amount of  $\text{CeO}_2$  uptake by ICP-OES (Figure 7B). Assessment of the Ce content in 120 dpf larvae exposed to C1 and C5 nanoparticles, demonstrated that, immediately following larval exposure for 6 hr, the animals exposed to C1 contained 14.52  $\mu\text{g}$  Ce per g of larval body weight while those exposed to C5 contained 14.34  $\mu\text{g}$  Ce per g of larval body weight. Repeat of the ICP-OES analysis in 144 hpf larvae, 24 hr after a 6 hr exposure, showed a steep decline in both C1 and C5 Ce content, suggesting

that most of the material was cleared from the GIT. This was also confirmed by light optical microscopy. TEM analysis of the pseudo-feces collected at the bottom of the aquarium tanks confirmed the presence of CeO<sub>2</sub> agglomerates (Figure S5). In accordance with the requirement of GIT uptake by the mouth, embryos lacking an oral aperture (24 and 72 hpf) had no discernible Ce uptake.

### Assessment of GIT Damage by LAR CeO<sub>2</sub> Nanoparticles

Since the GIT is the main target organ for CeO<sub>2</sub> nanoparticles at the larval stage, histological and TEM analyses were performed in zebrafish exposed to C1 and C5 nanoparticles 3 days after the third pulse exposure (*i.e.*, 14 dpf). H&E staining revealed clear evidence of structural damage by C5 but not C1. Specifically, C5 ingestion was associated with desquamation of the enterocytes and development of a vacuolar appearance in the intestinal lining (Figure 8A). TEM analysis of a GIT section confirmed the presence of C5-associated ultrastructural damage, which showed up as blunting of microvilli and epithelial atrophy (Figure 8B). Bundles of the LAR nanoparticles could be seen to pierce and disrupt the structure of microvilli (Figure 8C, Figure S6A and B). However, in spite of this damage, C5 nanorods could not be seen to be directly taken up into epithelial cells or gain access to subepithelial tissue. Instead, the C5 nanorods passed through the GIT and appeared in the pseudo-feces (Figure S5A and B). In contrast, C1 was not associated with any damage to the closely stacked microvilli, in spite of nanoparticle adherence to the tips of the microvilli (Figure 8C).

In order to reconcile the structural GIT damage with the developmental abnormalities depicted in Figures 6B–E, we asked whether this was due to interference in digestive function. In order to test digestive function, we used an *in vivo* fluorescence-based technique to monitor the digestion of an intramolecular-quenched protein (EnzChek).<sup>41–42</sup> EnzChek was fed to the larvae a day after exposure to CeO<sub>2</sub> nanoparticles. Digestion of this protein releases fluorescent peptides, which can be quantitatively assessed by fluorescence spectroscopy (Figure 9A) or the use of ImageJ software that analyzes fluorescence microscopy images in intact larvae (Figure 9B, left panel). Scoring of the fluorescence intensity by ImageJ analysis demonstrated that C5, but not C1 or C3, could induce a decrease in fluorescence intensity in the GIT of exposed larvae (Figure 9B, right panel). This confirms that C5 nanorods can induce GIT damage, leading to digestive malfunction and developmental abnormalities.

## DISCUSSION

In this study, we compared the *in vivo* effects of LAR CeO<sub>2</sub> nanoparticles with nanospheres in the murine lung as well as a zebrafish intestinal tract. The oropharyngeal aspiration studies in the mice showed that at a dose of 4 mg/Kg, all CeO<sub>2</sub> nanoparticles induced fibrogenic effects in the lung, culminating in pulmonary fibrosis 44 days later. However, if corrected for the higher lung burden of the nanospheres, the material with the longest AR material (C5) induced more fibrosis than the spheres (C1). The ability of LAR CeO<sub>2</sub> (C5) to induce IL-1 $\beta$  and TGF- $\beta$ 1 production in the lung at supra-threshold amounts may play a role in the fibrogenic effects of these materials. This agrees with the structure-activity

relationship (SAR) analysis in THP-1 cells and BMDMs, where LAR injury is accompanied by NLRP3 assembly and IL-1 $\beta$  production. C5 nanorods also resulted in prominent injury to the GIT of zebrafish larvae, while shorter rods or spherical nanoparticles had no effect. The mechanistic basis of this injury appears to be the ability of C5 to damage the microvilli, resulting in digestive malfunction, nutritional deficiency, retarded growth and abnormal physical development. Interestingly, the C5 nanorods did not differ from the nanospheres with respect to nanoparticle uptake and retention kinetics in the GIT. All considered, these results demonstrate the importance of CeO<sub>2</sub> AR in occupational and environmental hazard assessment.

The pulmonary hazard potential of CeO<sub>2</sub> is an important consideration based on the dispersive nature of these materials, which are being used as additives for fossil fuel combustion, polishing of material surfaces and biomedical devices.<sup>11, 43</sup> Mining of rare earth (RE) metals, of which cerium is a major ingredient (80%), has also been reported to be associated with an occupational pneumoconiosis, characterized by granulomatous inflammation and interstitial fibrosis.<sup>44–45</sup> Moreover, tracheal instillation studies in rats have shown that spherical CeO<sub>2</sub> nanoparticles can induce lung fibrosis in a dose and time-dependent manner.<sup>7, 11, 44–45</sup> While the mechanism(s) of the pro-fibrogenic effects is/are uncertain, it has been suggested that CeO<sub>2</sub> particles generate ROS and oxidative stress that could be involved in lung injury.<sup>7, 46–47</sup> However, compared to a list of more toxic metal oxide nanoparticles, we have found CeO<sub>2</sub> to be relatively inert in terms of oxidant injury in the lung, in addition to literature reporting CeO<sub>2</sub>'s antioxidant effects as a result of difference in valence state.<sup>7, 48–50</sup> Another biological injury could occur due to the high binding affinity of rare earth oxides for cellular phosphate groups, including membrane phospholipids and cellular phosphoproteins.<sup>51</sup> However, CeO<sub>2</sub> did not exhibit a strong effect in this regard compared to effect other rare earth oxides.<sup>51</sup> Similar to the studies of pro-fibrogenic potential of CeO<sub>2</sub> in the rat lung,<sup>11</sup> collagen deposition in the mouse lung was accompanied by TGF- $\beta$ 1 production. TGF- $\beta$ 1 is a pro-fibrogenic growth factor that is produced as a component of a lung fibrosis cascade that commences during an early stage as IL-1 $\beta$  production in activated pulmonary macrophages. Activated macrophages cooperate with pulmonary epithelial cells, which transition to mesenchymal cells and fibroblasts depositing collagen in the lung.<sup>25–26, 52</sup> Our previous study and this communication indicate that the AR of the CeO<sub>2</sub> nanoparticles plays a role in these trophic cellular interactions by triggering a pathway that involves lysosomal damage and NLRP3 inflammasome activation.<sup>6</sup> Moreover, we have previously demonstrated that there is a specific threshold above which the AR triggers lysosomal damage and NLRP3 assembly, as confirmed by the data in Figure S1A and 1B. Pertaining to the particles used in this study, it is interesting that the length of the C5 stacking bundles (0.75 to 2  $\mu$ m) exceeds the lysosomal diameter, which varies from ~1.1 to 2.9  $\mu$ m.<sup>6, 53</sup> We propose, therefore, that above a dose of 2 mg/Kg, LAR dimension contributes to IL-1 $\beta$  production and determines the extent of pulmonary fibrosis. It is interesting that the CeO<sub>2</sub> nanospheres are better retained in the lung than C5 nanorods and that the contribution of the AR contribution could only be seen to emerge if the collagen content is corrected for Ce lung burden (Figure 5E). The higher lung burden of the spheres and/ could be due to more lung uptake, but could also result from lower bioavailability or higher clearance rate of C5.<sup>23, 54</sup> Another unique accomplishment of this work was the



demonstration of a good correlation between the pro-fibrogenic effects and *ex vivo* cellular responses for LAR CeO<sub>2</sub> nanorods. These findings suggest that the increased propensity towards NLRP3 inflammasome activation and IL-1 $\beta$  production at cellular level is predictive of a higher likelihood of chronic lung injury.

There is a relative paucity of data for cross-species or cross-taxa comparison of the injurious effects of nanomaterials in general and for LAR materials in particular. The importance of interspecies assessment of nanoparticle toxicology was recently proposed by Stone *et al.*,<sup>55</sup> because there is insufficient data or mechanistic understanding of nanomaterial hazard across taxa. As a rule, most studies are exclusively conducted in either a mammalian or an aquatic system, and do not pick up the unique structure-activity relationships that we show for CeO<sub>2</sub> nanorods in the mouse lung vs. the zebrafish GIT. Although the injury mechanism in the zebrafish did not appear to be associated with the same lysosomal damage as in the lung of mice, a novel mechanism showing micro villus injury emerged in the former organism. Our study is a promising step toward future SAR developments to predict the toxicity of engineered nanomaterials across different taxa.

While zebrafish larvae corroborate the importance of AR, the target is the GIT at a development stage during which the animals can ingest the C5 nanorods. In contrast, no effect is seen in larvae without a mouth or embryos (not shown) in which the pore sizes in the chorion are too small to allow particles access to the chorionic sac.<sup>12-13</sup> This notion is further supported by ICP-OES showing that Ce uptake in 1-day old embryos is only marginally higher than the threshold detection limit (Figure 6). In contrast, CeO<sub>2</sub> exposure after the zebrafish larvae developed a mouth organ (5 dpf)<sup>56</sup> leads to GIT uptake and epithelial injury. This explains why larvae exposed to C5 nanorods are stunted in growth and exhibit developmental abnormalities. Because larvae less than 14 days old do not display functional gills,<sup>57-58</sup> the GIT is the primary target organ for immersed particulates.<sup>59-60</sup> Different from the pulmonary uptake in mice, there are no differences in the retention of CeO<sub>2</sub> nanorods and nanospheres in the GIT of zebrafish larvae, with most of the ingested materials being cleared within 24 hr (Figure 7B). This suggests that the epithelial injury by the C5 nanorods occurs during passage through the GIT rather than adsorption in the GIT. How exactly the microvilli are damaged is unclear but does not appear to involve a lysosomal mechanism as in the lung. These data showing LAR effects in zebrafish are novel and also provide a novel structure-activity relationship that differs from the lung.

Although this study was not intended to provide a direct comparison of zebrafish with human pathology, the findings in the larvae do raise the question whether LAR nanomaterials may be involved in GIT damage in humans. This is significant from the perspective that engineered nanomaterials are increasingly being used in food as colorants, adhesives or anticaking agents.<sup>5,61</sup> Thus, gastrointestinal exposure to engineered nanomaterials is increasing in frequency.<sup>62-63</sup> Lomer *et al.* suggested that the average human ingest up to 10<sup>12</sup> micro- or nanoparticles per day.<sup>64</sup> Although GIT exposure to engineered nanoparticles may not have consequences in healthy individuals, there are some preliminary evidence that people with compromised GIT function (such as Crohn's disease) might have a higher risk when exposed to particulate substances in food.<sup>64</sup> GIT exposure could also originate in the respiratory tract because most particulates being cleared from the

lung by mucociliary transport are swallowed.<sup>7</sup> Oral administration of engineered nanomaterials are also increasingly being used for drug delivery and bioimaging.<sup>65</sup> Based on these observations, we will extend our studies on LAR CeO<sub>2</sub> to the mammalian GIT. Preliminary experiments in a human enterocyte cell line (Caco-2) have shown that C4 and C5 nanorods do induce lysosomal injury, similar to what we see in macrophages(unpublished data).

It is important to mention the limitations of our study. First, in the absence of relevant occupational or environmental exposure data, it is not possible to extrapolate our data to the dose response calculations that we could make for carbon nanotubes or Ag nanoparticles, where some occupational exposure data were available.<sup>26, 66</sup> We also have no idea about environmental exposure or predictive environmental concentrations of CeO<sub>2</sub> nanoparticles. Nonetheless, we should be able to use the platforms and methodologies developed in this study for the hazard assessment and estimating no-effect concentrations of LAR nanomaterials. Second, due to logistic limitations, the temporal analysis of CeO<sub>2</sub> bioavailability, onset of histological abnormalities, and development of toxicological manifestations could only be performed at limited time points. Nonetheless, the AR-dependent toxicological profiling of CeO<sub>2</sub> could be clearly demonstrated in both models.

## CONCLUSION

We demonstrate that in addition to material composition, the AR of CeO<sub>2</sub> nanoparticles contribute to toxicological injury in the murine lung and the zebrafish GIT. Moreover, we demonstrate that the structure-activity analysis for CeO<sub>2</sub> nanorods at the subcellular level is predictive of toxicological outcome in the murine lung after correction for lung burden and dose. However, while the predictions of lysosome injury in the myeloid cells and macrophages could help to predict the generation of fibrogenic responses in the mouse lung, damage to microvilli in the GIT of zebrafish larvae does not appear to be premised on lysosomal injury.

## MATERIALS AND METHODS

### Materials and Reagents

The CeO<sub>2</sub> nanomaterials used for this study was freshly synthesized by the same hydrothermal method described previously.<sup>6</sup> The intramolecular-quenched protein, EnzChek, was purchased from Invitrogen (E6639), and was dissolved in 0.1 M sodium bicarbonate (pH 8.3) at 1 mg/mL before aliquoting and storing at -20 °C. Working stock concentrations of EnzChek (20 µg/mL) was prepared by diluting the stock solution 50x in Holtfreter's medium. Calcein was purchased from Sigma Aldrich (C0875), and was dissolved in Holtfreter's medium at 1 mg/mL before aliquoting and storing at -20 °C. The working concentration of calcein was 20 µg/mL.

### Physicochemical Characterizations of CeO<sub>2</sub> Library Materials

The primary diameter and length of CeO<sub>2</sub> nanomaterials were determined by transmission electron microscopy (TEM), while the suspended particles were used for assessment of hydrodynamic size and surface charge. CeO<sub>2</sub> nanomaterials were dispersed in deionized

water by vortexing and bath sonication to yield a stock solution of 5 mg/mL as previously described.<sup>8</sup> The hydrodynamic sizes of the CeO<sub>2</sub>, dispersed in deionized water, DMEM cell culture medium (supplemented with 10 % FBS), and Holtfreter's medium (supplemented with 100 µg/mL alginate), were determined by high throughput dynamic light scattering (HT-DLS, Dynapro Plate Reader, Wyatt Technology), as described by Ji *et al.*<sup>67</sup> The surface charge of CeO<sub>2</sub> was determined by a ZetaPALS instrument (Brookhaven Instruments, Holtsville, NY). The ζ-potential was derived using the Helmholtz-Smoluchowski equation based on the measurements of the electrophoretic mobility of CeO<sub>2</sub> in deionized water and Holtfreter's medium.

### Cellular Culture and Co-incubation with CeO<sub>2</sub> nanorods

THP-1 cells were suspended in RPMI 1640 medium supplemented with 10 % fetal bovine serum in 75 cm<sup>2</sup> flasks. Before exposure to CeO<sub>2</sub> nanoparticles, THP-1 cells were pretreated with 1 µg/mL phorbol 12-myristate acetate (PMA) overnight and primed with 10 ng/mL lipopolysaccharide (LPS). Aliquots of 3 × 10<sup>4</sup> primed cells were cultured in 0.1 mL medium with CeO<sub>2</sub> nanoparticles in 96-well plates (Costar, Corning, NY, USA) at 37 °C for 24 h. All the CeO<sub>2</sub> nanoparticle suspensions were freshly prepared. After 24 h, the supernatants were collected for the measurement of IL-1β activity (BD Biosciences, San Diego, CA) using ELISA kits according to manufacturer's instructions. Concentrations were expressed as pg/mL.

Bone marrow-derived macrophages (BMDMs) were differentiated in DMEM with 10% endotoxin-free fetal bovine serum and 20 % M-CSF-conditioned medium for 7 days, then plated at ~1.0 × 10<sup>6</sup> cells/mL and cultured for 2 days. BMDMs were primed with 500 ng/mL LPS for 5 h and then treated with the CeO<sub>2</sub> nanoparticles. After 24 h of culture, the supernatants were collected for the measurement of IL-1β activity using the ELISA kit described above.

### Assessment of Toxicological Responses in the Mouse Lung by Oropharyngeal Aspiration

Eight week old male C57BL/6 mice were purchased from Charles River Laboratories (Hollister, CA). All animals were housed under standard laboratory conditions established by the UCLA and NIH Guidelines for the Care and Use of Laboratory Animals in Research (DHEW78-23). Experimentation was approved by the Chancellor's Animal Research Committee at UCLA and include standard operating procedures for animal housing (filter-topped cages; room temperature at 23 ± 2 °C; 60 % relative humidity; 12 h light, 12 h dark cycle) and hygiene status (autoclaved food and acidified water). Animal exposure to CeO<sub>2</sub> nanoparticles was carried out by oropharyngeal aspiration as described previously. Briefly, the animals were anesthetized by intraperitoneal injection of ketamine (100 mg/Kg)/xylazine (10 mg/Kg) in a total volume of 100 µL. With the anesthetized animals held in a vertical position, 50 µL suspensions containing the particles at 10, 20, 40 and 80 µg in PBS (equivalent to 0.5, 1.0, 2.0 and 4.0 mg/Kg) were instilled at the back of the tongue to allow aspiration to the lung as described previously.<sup>68</sup> We used 6 animals per group. Control animals received the same volume of PBS. The positive control group in each experiment was comprised of animals receiving 5.0 mg/Kg quartz (Min-U-Sil®, QTZ). The mice were sacrificed at 40 h, 21 d or 44 d post-exposure and BALF and lung tissues were collected.

The BALF was used to perform total and differential cell counts and to measure the levels of LIX, IL-1 $\beta$ , and TGF- $\beta$ 1. Lung sections were stained with hematoxylin/eosin or with Masson's trichrome to visualize collagen deposition. LIX, IL-1 $\beta$  (BD Biosciences, San Diego, CA) and TGF- $\beta$ 1 (Promega, Madison, WI) levels in the BALF were analyzed using ELISA kits according to manufacturer's instructions. Concentrations were expressed as pg/mL.

### Sircol Assay for Total Collagen Production in lung tissue

The right cranial lobe of each lung was suspended in PBS at ~50 mg tissue/mL and homogenized for 60 s with a tissue homogenizer (Fisher Scientific). Acetic acid was added to each sample to a final concentration of 0.5 M and incubated at 4 °C overnight. Cellular debris was removed by centrifugation and the supernatant analyzed for total protein, using a BCA assay kit (Pierce/ThermoFisher Scientific). The Sircol soluble collagen assay kit (Biocolor Ltd., Carrickfergus, UK) was used to extract collagen from duplicate samples using 200  $\mu$ L of supernatant and 800  $\mu$ L dye reagent according to the manufacturer's instructions. Similarly prepared collagen standards (10~50  $\mu$ g) were run in parallel. Collagen pellets were washed twice with denatured alcohol and dried before suspension in alkali reagent. Absorbance at 555 nm was read on a plate reader (SpectroMax M5e, Molecular Devices Corp., Sunnyvale, CA). Data were expressed as  $\mu$ g soluble collagen per mg of total protein.

### Pulse-Exposure of Zebrafish Larvae and Assessment of Health Status

The developmental stages of zebrafish embryos and larvae were determined according to the published procedure of Kimmel *et al.*<sup>69</sup> For pulse exposure, groups of 30 growth-synchronized larvae at day 5 post-fertilization (5 dpf) were immersed in 3 mL 25 ug/mL CeO<sub>2</sub> suspensions in petri dishes for 6 hr at 28.5 °C. Following pulse exposure, the developing larvae were carefully washed in Holtfreter's medium 3 times before being placed in standard aquarium tanks (3L) for regular feeding and water circulation. The second and third pulse exposures were conducted on the same larvae at 8 and 11 dpf. Following that, the larvae were maintained in standard aquarium tanks for further observation of development and survival. In order to minimize the individual differences among larvae, larvae used in each replicate experiment were produced by the same adult breeding pair.

The overall health status of the larvae was assessed at 14 dpf based on gross morphology, body length and weight, and number of calcified vertebrae. To assess morphology, larvae were anesthetized in 0.02 % tricaine and embedded in low-melt agarose gel. This allowed positioning to obtain lateral views to assess morphology, body length, and fin structure. The images were captured using an optical inverted microscope (Zeiss Observer D1). For body weight measurement, larvae were anesthetized, dried with Kim wipes, and measured using a digital balance (Denver Instrument, XP-600). The larval weights for each treatment group were normalized to the control group and plotted as weight percentage. For the measurement of calcified vertebrae, larvae were immersed in a 20 ug/mL calcein solution for 30 minutes at 28.5 °C. After immersion, larvae were washed 3 times in Holtfreter's medium to remove non-specific staining and then embedded in low-melt agarose gel to obtain lateral views. The numbers of calcified vertebrates were counted based on the fluorescent images captured

under a fluorescence microscope equipped with 495/515 nm filter set (Zeiss Observer D1). The average number of calcified vertebrae from ten randomly selected larvae was compared to control, AgNPs and CeO<sub>2</sub> exposed groups.

### Confocal Raman Microscopy Analysis

Confocal Raman microscopy was performed using a Renishaw In Via model with a 514.5 nm Argon laser. The laser power and beam size were ~2.5 mW and 1 μm, respectively. The Raman spectra were collected from 0 to 2000 cm<sup>-1</sup> for all sample characterizations. For spectra collection, CeO<sub>2</sub> suspensions were dropped directly onto a glass cover slip before drying. For scanning, larvae were anesthetized and placed on a glass slide with concavity wells. The lateral view was desired for capturing full-length GIT images. Line scanning to collect Raman scattering signals was achieved by programming the motorized sample stage to move 1 μm in either x or y-axis direction stepwise.

### ICP-OES Analysis to Determine Ce Content in the Mouse Lung and Zebrafish Larvae

The total Ce content of the lungs of mice exposed for 44 days were collected and rinsed three times with PBS. Subsequently, the lung tissues were homogenized for 60 s with a tissue homogenizer (Fisher Scientific). The probe was washed with 500 μL PBS, which was added to the homogenate. All the homogenates were transferred to Teflon containers and acidified with 5 mL of 100 % ultrahigh purity nitric acid and digested at 95 °C for 3 hr before drying and re-dissolving in 5 % nitric acid. After digestion, the elemental Ce concentration in each sample was determined by a Shimadzu ICP-OES based on a calibration curve established by a series of concentrations of Ce standard solution (0.01 ppm ~ 10 ppm) and expressed as μg of Ce/mg of cellular protein.

ICP-OES analysis was performed on zebrafish embryos and larvae exposed to 25 μg/mL C1 and C5 for 6 hr at developmental stages 24, 72, 120 hpf as well as 24 hr after exposure in the 120 hpf group. Each exposure group included 50 embryos or larvae, which were thoroughly washed 3 times in Holtfreter's medium before subjecting to acid digestion as discussed above. The elemental Ce concentrations (weight/volume) were measured and expressed as μg of Ce/g of fish body weight. Groups of embryos and larvae without exposure to CeO<sub>2</sub> were anesthetized and weighted using a digital balance (Denver Instrument, XP-600) for calculating the fish body weight. To achieve reliable statistical analysis, three replicates were used for each group.

### TEM Analysis of the GIT of Exposed Zebrafish Larvae

TEM analysis of the GIT was conducted on 5 dpf larvae, immediately after the first CeO<sub>2</sub> exposures (for 6 hr) as well as 14 dpf (*i.e.*, 3 days after the 3<sup>rd</sup> CeO<sub>2</sub> exposure). The larvae were euthanized in tricaine and the GIT was micro-dissected before immersion in a 0.1M cacodylate buffer (that includes 2% glutaraldehyde and 2% paraformaldehyde at pH 7.4), for 2 hr at room temperature and then 4°C overnight. The samples were subsequently washed in 0.1M PBS buffer and post-fixed in a solution containing 1% OsO<sub>4</sub> for 2 hr at room temperature. After dehydration in graded ethanol (50%, 75%, 95%, 100%, 100%, 100%), the tissue samples were infiltrated in mixtures of Epon 812 and ethanol (1:1 ratio) and 2:1 for two hr each. The tissue samples were then incubated in pure Epon 812 overnight,

embedded and cured at 60°C for 48 hr. Sections of 55–65 nm thickness (gray interference color) were cut on an ultramicrotome (RMC MTX) that utilizes a diamond knife. The sections were deposited on single-hole copper grids coated with Formvar and double-stained with an 8% uranyl acetate solution at 60°C for 25 minutes, as well lead citrate for 3 minutes at room temperature. Thin sections were subsequently examined with a 100CX JEOL electron microscope in the Electron Microscopy Services Center of the UCLA Brain Research Institute.

### **Histological Analysis of Zebrafish Larvae**

Histological analysis was conducted on the developing larvae at 14 dpf. Larvae were euthanized in tricaine and fixed in 4% paraformaldehyde, first for 1 hr at room temperature and then overnight at 4 °C. After fixation, the larvae were embedded in histological gel and positioned in the lateral orientation view. The samples were further processed for resin embedding, sagittal sectioning, and Hematoxylin and Eosin (H&E) staining in the Pathology and Laboratory Medicine. High-resolution images (both 20X and 40X) of the histological sections were obtained using an automated scanning system (scanning Aperio ScanScope AT).

### **Assessment of digestive function in the zebrafish gut**

Larvae at 6 dpf (24 hr after 1<sup>st</sup> exposure) were immersed in the EnzChek solution at 20 µg/mL for 2 hr at 28.5 °C. The larvae were gently washed 3 times in Holtfreter's medium, anesthetized, and positioned in lateral views orientation in low-melt agarose gel on a glass bottom dish. The fluorescence images were captured by a fluorescence microscope (Zeiss Observer D1) with a 575/620 nm filter set. The images were further analyzed by ImageJ software (NIH).

### **Zebrafish Husbandry**

Wild type adult zebrafish (*Danio rerio*, AB strain) were housed and maintained in the UCLA zebrafish facility on a 14:10D photoperiod. Two pairs of male/female fish were placed in a single cage a day ahead of time and released the next morning to trigger spawning. The embryos were collected at 2 hpf and rinsed with Holtfreter's solution to remove any residue on the chorion. The embryos were subsequently examined under a stereomicroscope (Zeiss, Stemi 2000) for viability and developmental stage before being subjected to embryo screening and larvae experiments. All procedures were carried out in accordance with the Animal Care and Use Committee guidelines at UCLA.

### **Statistical Methods**

Results were statistically analyzed using two-side Student's t -test. The difference is regarded statistically significant if the p value is less than 0.05. Data are reported as the mean ± standard deviation from at least three separate experiments.

### **Supplementary Material**

Refer to Web version on PubMed Central for supplementary material.

## Acknowledgments

The studies on the mouse lung and the development of the CeO<sub>2</sub> nanoparticle library were primarily supported by U19 ES019528 and RO1 ES016746. The studies on the zebrafish larvae were supported by UC CEIN funding from the National Science Foundation and the Environmental Protection Agency under Cooperative Agreement Number DBI 1266377. Any opinions, findings, and conclusions or recommendations expressed in this material are those of the author(s) and do not necessarily reflect the views of the National Science Foundation or the Environmental Protection Agency. This work has not been subjected to EPA review and no official endorsement should be inferred.

## References

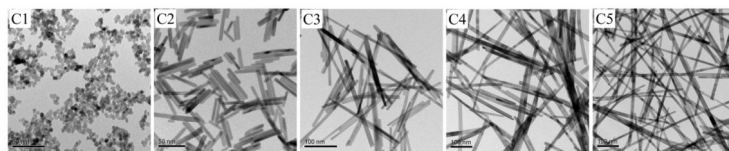
1. Huynh WU, Dittmer JJ, Alivisatos AP. Hybrid Nanorod-Polymer Solar Cells. *Science*. 2002; 295:2425–2427. [PubMed: 11923531]
2. Jana NR, Gearheart L, Murphy CJ. Wet Chemical Synthesis of High Aspect Ratio Cylindrical Gold Nanorods. *J Phys Chem B*. 2001; 105:4062–4067.
3. Murphy CJ, Jana NR. Controlling the Aspect Ratio of Inorganic Nanorods and Nanowires. *Adv Mater*. 2002; 14:80–82.
4. Nakayama K, Kubo T, Nishikitani Y. Anodic Formation of Titania Nanotubes with Ultrahigh Aspect Ratio. *Electrochem Solid St*. 2008; 11:C23–C26.
5. Duncan TV. Applications of Nanotechnology in Food Packaging and Food Safety: Barrier Materials, Antimicrobials and Sensors. *J Colloid Interf Sci*. 2011; 363:1–24.
6. Ji Z, Wang X, Zhang H, Lin S, Meng H, Sun B, George S, Xia T, Nel AE, Zink JJ. Designed Synthesis of CeO<sub>2</sub> Nanorods and Nanowires for Studying Toxicological Effects of High Aspect Ratio Nanomaterials. *ACS Nano*. 2012; 6:5366–5380. [PubMed: 22564147]
7. Cassee FR, van Balen EC, Singh C, Green D, Muijsers H, Weinstein J, Dreher K. Exposure, Health and Ecological Effects Review of Engineered Nanoscale Cerium and Cerium Oxide Associated with Its Use as a Fuel Additive. *Cr Rev Toxicol*. 2011; 41:213–229.
8. Zhang J, Ju X, Wu ZJ, Liu T, Hu D, Xie YN. Structural Characteristics of Cerium Oxide Nanocrystals Prepared by the Microemulsion Method. *Chem Mater*. 2001; 13:4192–4197.
9. Mai HX, Sun LD, Zhang YW, Si R, Feng W, Zhang HP, Liu HC, Yan CH. Shape-Selective Synthesis and Oxygen Storage Behavior of Ceria Nanopolyhedra, Nanorods, and Nanocubes. *J Phys Chem B*. 2005; 109:24380–24385. [PubMed: 16375438]
10. Zhou K, Yang Z, Yang S. Highly Reducible CeO<sub>2</sub> Nanotubes. *Chem Mater*. 2007; 19:1215–1217.
11. Ma JY, Mercer RR, Barger M, Schwegler-Berry D, Scabilloni J, Ma JK, Castranova V. Induction of Pulmonary Fibrosis by Cerium Oxide Nanoparticles. *Toxicol Appl Pharm*. 2012; 262:255–264.
12. Lin S, Zhao Y, Xia T, Meng H, Ji Z, Liu R, George S, Xiong S, Wang X, Zhang H, et al. High Content Screening in Zebrafish Speeds up Hazard Ranking of Transition Metal Oxide Nanoparticles. *ACS Nano*. 2011; 5:7284–7295. [PubMed: 21851096]
13. Lin S, Zhao Y, Ji Z, Ear J, Chang CH, Zhang H, Low-Kam C, Yamada K, Meng H, Wang X, et al. Zebrafish High-Throughput Screening to Study the Impact of Dissolvable Metal Oxide Nanoparticles on the Hatching Enzyme, ZHE1. *Small*. 2013; 9:1776–1785. [PubMed: 23180726]
14. Lin S, Zhao Y, Nel AE, Lin S. Zebrafish: An *in vivo* Model for Nano EHS Studies. *Small*. 2012; 9:1608–1618. [PubMed: 23208995]
15. Meng H, Xia T, George S, Nel AE. A Predictive Toxicological Paradigm for the Safety Assessment of Nanomaterials. *ACS Nano*. 2009; 3:1620–1627. [PubMed: 21452863]
16. Bonner JC, Silva RM, Taylor AJ, Brown JM, Hilderbrand SC, Castranova V, Porter D, Elder A, Oberdorster G, Harkema JR, et al. Interlaboratory Evaluation of Rodent Pulmonary Responses to Engineered Nanomaterials: The NIEHS Nano Go Consortium. *Environ Health Persp*. 2013; 121:676–682.
17. Nel AE, Xia T, Meng H, Wang X, Lin S, Ji Z, Zhang H. Nanomaterials Toxicity Testing in the 21st Century: Use of a Predictive Toxicological Approach and High-Throughput Screening. *Acc Chem Res*. 2012; 46:607–621. [PubMed: 22676423]

18. Hamilton RF, Wu N, Porter D, Buford M, Wolfarth M, Holian A. Particle Length-Dependent Titanium Dioxide Nanomaterials Toxicity and Bioactivity. *Part Fibre Toxicol.* 2009; 6:35. [PubMed: 20043844]
19. Porter DW, Wu N, Hubbs AF, Mercer RR, Funk K, Meng F, Li J, Wolfarth MG, Battelli L, Friend S, et al. Differential Mouse Pulmonary Dose and Time Course Responses to Titanium Dioxide Nanospheres and Nanobelts. *Toxicol Sci.* 2013; 131:179–193. [PubMed: 22956629]
20. Donaldson K, Murphy F, Schinwald A, Duffin R, Poland CA. Identifying the Pulmonary Hazard of High Aspect Ratio Nanoparticles to Enable Their Safety-by-Design. *Nanomedicine.* 2011; 6:143–156. [PubMed: 21182425]
21. Tomatis M, Turci F, Ceschino R, Riganti C, Gazzano E, Martra G, Ghigo D, Fubini B. High Aspect Ratio Materials: Role of Surface Chemistry vs. Length in the Historical “Long and Short Amosite Asbestos Fibers”. *Inhal Toxicol.* 2010; 22:984–998. [PubMed: 20718637]
22. Oberdörster G, Stone V, Donaldson K. Toxicology of Nanoparticles: A Historical Perspective. *Nanotoxicology.* 2007; 1:2–25.
23. Blake T, Castranova V, Schwegler-Berry D, Baron P, Deye GJ, Li CH, Jones W. Effect of Fiber Length on Glass Microfiber Cytotoxicity. *J Toxicol Env Heal A.* 1998; 54:243–259.
24. Li RB, Wang X, Ji ZX, Sun BB, Zhang HY, Chang CH, Lin SJ, Meng H, Liao YP, Wang MY, et al. Surface Charge and Cellular Processing of Covalently Functionalized Multiwall Carbon Nanotubes Determine Pulmonary Toxicity. *ACS Nano.* 2013; 7:2352–2368. [PubMed: 23414138]
25. Wang X, Xia T, Duch MC, Ji ZX, Zhang HY, Li RB, Sun BB, Lin SJ, Meng H, Liao YP, et al. Pluronic F108 Coating Decreases the Lung Fibrosis Potential of Multiwall Carbon Nanotubes by Reducing Lysosomal Injury. *Nano Lett.* 2012; 12:3050–3061. [PubMed: 22546002]
26. Wang X, Xia T, Ntim SA, Ji ZX, Lin SJ, Meng H, Chung CH, George S, Zhang HY, Wang MY, et al. Dispersal State of Multiwalled Carbon Nanotubes Elicits Profibrogenic Cellular Responses That Correlate with Fibrogenesis Biomarkers and Fibrosis in the Murine Lung. *ACS Nano.* 2011; 5:9772–9787. [PubMed: 22047207]
27. Rodea-Palomares I, Boltes K, Fernandez-Pinas F, Leganes F, Garcia-Calvo E, Santiago J, Rosal R. Physicochemical Characterization and Ecotoxicological Assessment of CeO<sub>2</sub> Nanoparticles Using Two Aquatic Microorganisms. *Toxicol Sci.* 2011; 119:135–145. [PubMed: 20929986]
28. Manier N, Garaud M, Delalain P, Aguerre-Chariol O, Pandard P. Behaviour of Ceria Nanoparticles in Standardized Test Media – Influence on the Results of Ecotoxicological Tests. *J Phys.* 2011; 304:012058.
29. Roberts AP, Mount AS, Seda B, Souther J, Qiao R, Lin S, Ke PC, Rao AM, Klaine SJ. *In vivo* Biomodification of Lipid-Coated Carbon Nanotubes by *Daphnia magna*. *Environ Sci Technol.* 2007; 41:3025–3029. [PubMed: 17533874]
30. Cheng J, Chan CM, Veca LM, Poon WL, Chan PK, Qu L, Sun YP, Cheng SH. Acute and Long-Term Effects after Single Loading of Functionalized Multi-Walled Carbon Nanotubes into Zebrafish (*Danio rerio*). *Toxicol Appl Pharm.* 2009; 235:216–225.
31. Smith CJ, Shaw BJ, Handy RD. Toxicity of Single Walled Carbon Nanotubes to Rainbow Trout, (*Oncorhynchus mykiss*): Respiratory Toxicity, Organ Pathologies, and Other Physiological Effects. *Aquat Toxicol.* 2007; 82:94–109. [PubMed: 17343929]
32. Fraser TW, Reinardy HC, Shaw BJ, Henry TB, Handy RD. Dietary Toxicity of Single-Walled Carbon Nanotubes and Fullerenes (C<sub>60</sub>) in Rainbow Trout (*Oncorhynchus mykiss*). *Nanotoxicology.* 2011; 5:98–108. [PubMed: 21417691]
33. Ispas C, Andreescu D, Patel A, Goia DV, Andreescu S, Wallace KN. Toxicity and Developmental Defects of Different Sizes and Shape Nickel Nanoparticles in Zebrafish. *Environ Sci Technol.* 2009; 43:6349–6356. [PubMed: 19746736]
34. Scanlan L, Reed RB, Loguinov AV, Antczak P, Tagmount A, Aloni S, Nowinski DT, Luong P, Tran C, Karunaratne N, et al. Silver Nanowire Exposure Results in Internalization and Toxicity to *Daphnia magna*. *ACS Nano.* 2013; 7:10681–10694. [PubMed: 24099093]
35. Asharani PV, Lian Wu Y, Gong Z, Valiyaveetil S. Toxicity of Silver Nanoparticles in Zebrafish Models. *Nanotechnology.* 2008; 19:255102. [PubMed: 21828644]



36. Powers CM, Yen J, Linney EA, Seidler FJ, Slotkin TA. Silver Exposure in Developing Zebrafish (*Danio rerio*): Persistent Effects on Larval Behavior and Survival. *Neurotoxicol Teratol*. 2010; 32:391–397. [PubMed: 20116428]
37. George S, Lin S, Ji Z, Thomas CR, Li L, Mecklenburg M, Meng H, Wang X, Zhang H, Xia T, et al. Surface Defects on Plate-Shaped Silver Nanoparticles Contribute to Its Hazard Potential in a Fish Gill Cell Line and Zebrafish Embryos. *ACS Nano*. 2012; 6:3745–3759. [PubMed: 22482460]
38. Du SJ, Frenkel V, Kindschi G, Zohar Y. Visualizing Normal and Defective Bone Development in Zebrafish Embryos Using the Fluorescent Chromophore Calcein. *Dev Biol*. 2001; 238:239–246. [PubMed: 11784007]
39. Rekhi S, Saxena SK, Lazor P. High-Pressure Raman Study on Nanocrystalline CeO<sub>2</sub>. *J Appl Phys*. 2001; 89:2968–2971.
40. Spanier J, Robinson R, Zhang F, Chan SW, Herman I. Size-Dependent Properties of CeO<sub>2</sub>-Y Nanoparticles as Studied by Raman Scattering. *Phys Rev B*. 2001; 64:245407.
41. Hama K, Provost E, Baranowski TC, Rubinstein AL, Anderson JL, Leach SD, Farber SA. *In vivo* Imaging of Zebrafish Digestive Organ Function Using Multiple Quenched Fluorescent Reporters. *Am J Physiol Gastrointest Liver Physiol*. 2009; 296:G445–G453. [PubMed: 19056761]
42. Otis JP, Farber SA. Imaging Vertebrate Digestive Function and Lipid Metabolism *in vivo*. *Drug Discov Today*. 2012; 10:e11–e16.
43. HEI - Health Effects Institute, R. R. HEI Research Communication 9. North Andover Ma: Flagship Press; 2001. Evaluation of Human Health Risk from Cerium added to Diesel Fuel. <http://pubs.healtheffects.org/view.php?id=172>
44. Waring PM, Watling RJ. Rare-Earth Deposits in a Deceased Movie Projectionist - a New Case of Rare-Earth Pneumoconiosis. *Med J Australia*. 1990; 153:726–730. [PubMed: 2247001]
45. McDonald JW, Ghio AJ, Sheehan CE, Bernhardt PF, Roggli VL. Rare-Earth (Cerium Oxide) Pneumoconiosis - Analytical Scanning Electron-Microscopy and Literature-Review. *Modern Pathol*. 1995; 8:859–865.
46. Eom HJ, Choi J. Oxidative Stress of CeO<sub>2</sub> Nanoparticles Via P38-Nrf-2 Signaling Pathway in Human Bronchial Epithelial Cell, Beas-2B. *Toxicol Lett*. 2009; 187:77–83. [PubMed: 19429248]
47. Yokel RA, Florence RL, Unrine JM, Tseng MT, Graham UM, Wu P, Grulke EA, Sultana R, Hardas SS, Butterfield DA. Biodistribution and Oxidative Stress Effects of a Systemically-Introduced Commercial Ceria Engineered Nanomaterial. *Nanotoxicology*. 2009; 3:234–248.
48. Zhang H, Ji Z, Xia T, Meng H, Low-Kam C, Liu R, Pokhrel S, Lin S, Wang X, Liao YP, et al. Use of Metal Oxide Nanoparticle Band Gap to Develop a Predictive Paradigm for Oxidative Stress and Acute Pulmonary Inflammation. *ACS Nano*. 2012; 6:4349–4368. [PubMed: 22502734]
49. Das M, Patil S, Bhargava N, Kang JF, Riedel LM, Seal S, Hickman JJ. Auto-Catalytic Ceria Nanoparticles Offer Neuroprotection to Adult Rat Spinal Cord Neurons. *Biomaterials*. 2007; 28:1918–1925. [PubMed: 17222903]
50. Perez JM, Asati A, Nath S, Kaittanis C. Synthesis of Biocompatible Dextran-Coated Nanoceria with Ph-Dependent Antioxidant Properties. *Small*. 2008; 4:552–556. [PubMed: 18433077]
51. Li R, Ji Z, Chang CH, Dunphy DR, Cai X, Meng H, Zhang H, Sun B, Wang X, Dong J, et al. Surface Interactions with Compartmentalized Cellular Phosphates Explain Rare Earth Oxide Nanoparticle Hazard and Provide Opportunities for Safer Design. *ACS Nano*. 2014; 8:1771–1783. [PubMed: 24417322]
52. Bonner JC. Mesenchymal Cell Survival in Airway and Interstitial Pulmonary Fibrosis. *Fibrogenesis Tissue Repair*. 2010; 3:15. [PubMed: 20738867]
53. McClure J, Cameron CHS, Garrett R. The Ultrastructural Features of Malakoplakia. *J Pathol*. 1981; 134:13–25. [PubMed: 6270293]
54. Donaldson K, Murphy FA, Duffin R, Poland CA. Asbestos, Carbon Nanotubes and the Pleural Mesothelium: A Review of the Hypothesis Regarding the Role of Long Fibre Retention in the Parietal Pleura, Inflammation and Mesothelioma. *Part Fibre Toxicol*. 2010; 7:5. [PubMed: 20307263]
55. Gaiser BK, Fernandes TF, Jepson MA, Lead JR, Tyler CR, Baalousha M, Biswas A, Britton GJ, Cole PA, Johnston BD, et al. Interspecies Comparisons on the Uptake and Toxicity of Silver and Cerium Dioxide Nanoparticles. *Environ Toxicol Chem*. 2012; 31:144–154. [PubMed: 22002553]

56. Ng AN, de Jong-Curtain TA, Mawdsley DJ, White SJ, Shin J, Appel B, Dong PD, Stainier DY, Heath JK. Formation of the Digestive System in Zebrafish: Iii. Intestinal Epithelium Morphogenesis. *Dev Biol.* 2005; 286:114–135. [PubMed: 16125164]
57. Rombough P. Gills Are Needed for Ionoregulation before They Are Needed for O<sub>2</sub> Uptake in Developing Zebrafish, *Danio Rerio*. *J Exp Biol.* 2002; 205:1787–1794. [PubMed: 12042337]
58. McLeish JA, Chico TJ, Taylor HB, Tucker C, Donaldson K, Brown SB. Skin Exposure to Micro- and Nano-Particles Can Cause Haemostasis in Zebrafish Larvae. *Thromb Haemostasis.* 2010; 103:797–807. [PubMed: 20174755]
59. Farkas J, Christian P, Urrea JA, Roos N, Hasselov M, Tollefsen KE, Thomas KV. Effects of Silver and Gold Nanoparticles on Rainbow Trout (*Oncorhynchus mykiss*) Hepatocytes. *Aquat Toxicol.* 2010; 96:44–52. [PubMed: 19853932]
60. Griffitt RJ, Brown-Peterson NJ, Savin DA, Manning CS, Boube I, Ryan RA, Brouwer M. Effects of Chronic Nanoparticulate Silver Exposure to Adult and Juvenile Sheepshead Minnows (*Cyprinodon variegatus*). *Environ Toxicol Chem.* 2012; 31:160–167. [PubMed: 21994144]
61. Chaudhry Q, Scotter M, Blackburn J, Ross B, Boxall A, Castle L, Aitken R, Watkins R. Applications and Implications of Nanotechnologies for the Food Sector. *Food Addit Contam A.* 2008; 25:241–258.
62. Hoet PH, Bruske-Hohlfeld I, Salata OV. Nanoparticles - Known and Unknown Health Risks. *J Nanobiotechnol.* 2004; 2:12.
63. Powell JJ, Faria N, Thomas-McKay E, Pele LC. Origin and Fate of Dietary Nanoparticles and Microparticles in the Gastrointestinal Tract. *J Autoimmun.* 2010; 34:J226–J233. [PubMed: 20096538]
64. Lomer MCE, Thompson RPH, Powell JJ. Fine and Ultrafine Particles of the Diet: Influence on the Mucosal Immune Response and Association with Crohn's Disease. *P Nutr Soc.* 2007; 61:123–130.
65. Uskokovic V, Lee K, Lee PP, Fischer KE, Desai TA. Shape Effect in the Design of Nanowire-Coated Microparticles as Transepithelial Drug Delivery Devices. *ACS Nano.* 2012; 6:7832–7841. [PubMed: 22900471]
66. Wang X, Ji Z, Chang CH, Zhang H, Wang M, Liao YP, Lin S, Meng H, Li R, Sun B, et al. Use of Coated Silver Nanoparticles to Understand the Relationship of Particle Dissolution and Bioavailability to Cell and Lung Toxicological Potential. *Small.* 2013; 10:385–398. [PubMed: 24039004]
67. Ji Z, Jin X, George S, Xia T, Meng H, Wang X, Suarez E, Zhang H, Hoek EMV, Godwin H, et al. Dispersion and Stability Optimization of TiO<sub>2</sub> Nanoparticles in Cell Culture Media. *Environ Sci Technol.* 2010; 44:7309–7314. [PubMed: 20536146]
68. Li N, Wang M, Bramble LA, Schmitz DA, Schauer JJ, Sioutas C, Harkema JR, Nel AE. The Adjuvant Effect of Ambient Particulate Matter Is Closely Reflected by the Particulate Oxidant Potential. *Environ Health Persp.* 2009; 117:1116–1123.
69. Kimmel CB, Ballard WW, Kimmel SR, Ullmann B, Schilling TF. Stages of Embryonic Development of the Zebrafish. *Dev Dynam.* 1995; 203:253–310.



Sample name	L (nm)	D (nm)	AR	Hydrodynamic diameter (nm)			zeta-potential (mV)		
				DI H <sub>2</sub> O	DMEM	Holtfreter's medium	DI H <sub>2</sub> O	DMEM	Holtfreter's medium
C1	N/A	7	1	56 ± 1	223 ± 3	805 ± 38	40.6 ± 2.2	-11.3 ± 3.0	-32.4 ± 1.4
C2	50.8	6.7	8	265 ± 3	444 ± 37	782 ± 48	38.2 ± 2.4	-11.1 ± 2.6	-31.6 ± 2.8
C3	197.2	9.1	22	449 ± 27	705 ± 59	1001 ± 23	31.6 ± 1.1	-11.1 ± 1.8	-19.72 ± 2.6
C4	495.7	9.5	52	643 ± 109	1382 ± 59	719 ± 10	32.7 ± 2.0	-15.3 ± 1.3	-24.92 ± 2.2
C5	>1000	9.5	>100	900 ± 41	1570 ± 238	1248 ± 71	11.7 ± 0.6	-10.4 ± 1.6	-32.55 ± 1.8

**Figure 1.** Physicochemical characterization of CeO<sub>2</sub> nanospheres and nanorods. (A) Representative TEM images show the primary size, shape, and AR of CeO<sub>2</sub> (C1, C2, C3, C4 and C5). (B) Table summarizing the diameter, length, and AR of CeO<sub>2</sub> based on the TEM analysis, as well as the hydrodynamic diameter and surface charge of nanoparticles suspended in distilled water, cell culture medium (DMEM) and zebrafish growth medium (Holtfreter's medium).

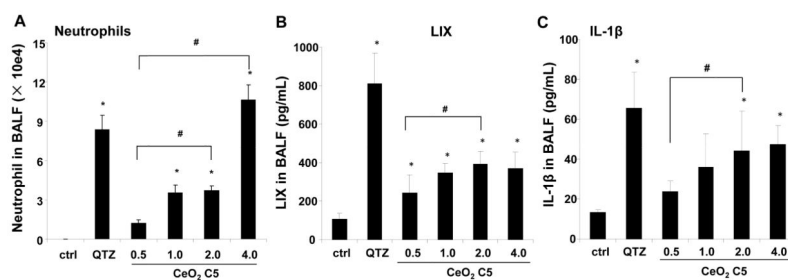


**Figure 2.**

Acute pulmonary effects of CeO<sub>2</sub> nanoparticles in C57BL/6 mice. The dose-dependent experiment was carried out in mice exposed to CeO<sub>2</sub> nanoparticles C5 at 0.5, 1.0, 2.0 and 4.0 mg/kg by oropharyngeal aspiration. There were 6 animals per group. Animals were euthanized after 40 hr, and BALF was collected to determine neutrophil cell counts (A), LIX (B) and IL-1 $\beta$  (C) levels. Animals exposed to 5.0 mg/kg QTZ were used as positive control. The experiment was reproduced a second time; \* p < 0.05 compared to control; # p < 0.05 for pairwise comparisons as shown.

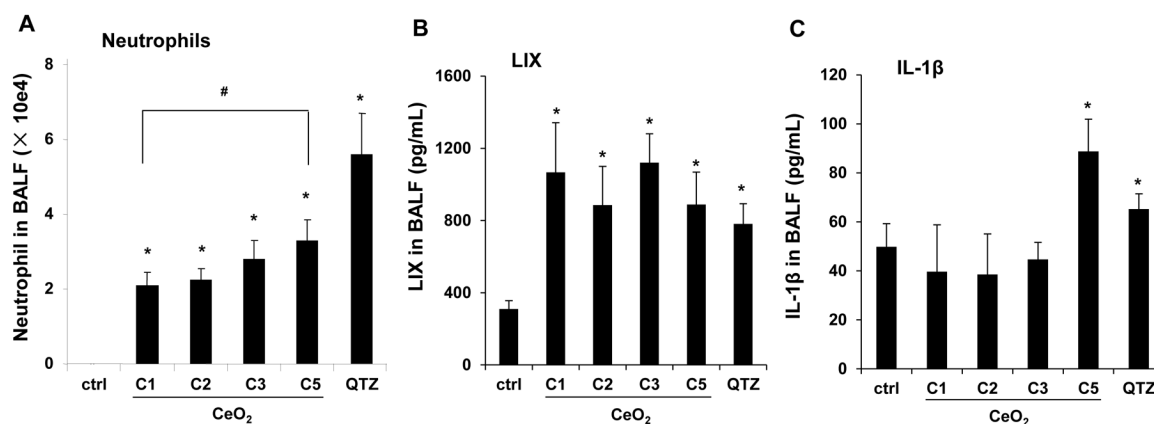


**Figure 3.**

Acute pulmonary effects of CeO<sub>2</sub> nanoparticles in mice. The comparison experiment was carried out in C57BL/6 mice exposed to CeO<sub>2</sub> nanoparticles C1, C2, C3 and C5 at 2.0 mg/Kg by oropharyngeal aspiration. There were 6 animals per group. Mice were sacrificed at 40 hr and the neutrophil cell counts (A), LIX (B) and IL -1 $\beta$  (C) levels in BALF were determined. QTZ at 5.0 mg/Kg was used as a positive control. The experiment was reproduced a second time; \*  $p < 0.05$  compared to control; #  $p < 0.05$  for pairwise comparisons as shown.

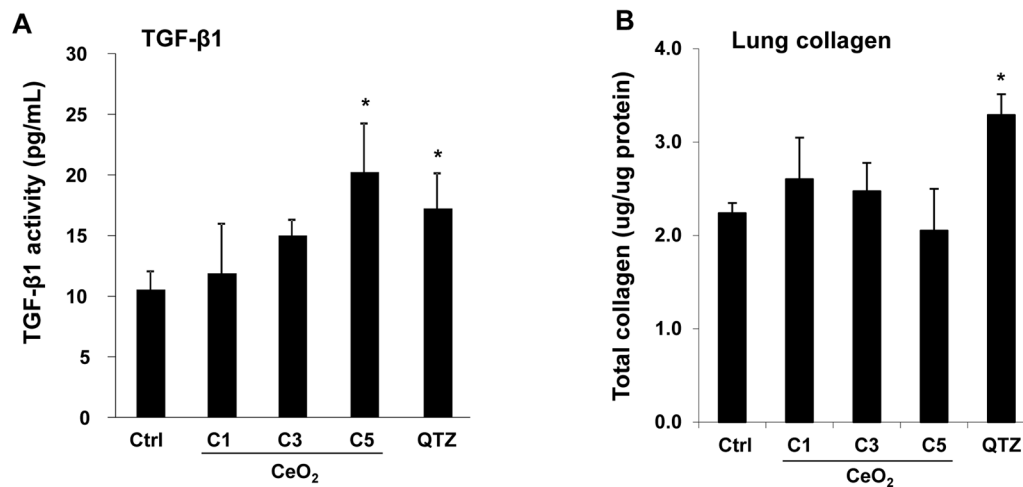


**Figure 4.** Sub-chronic pulmonary effects of CeO<sub>2</sub> nanoparticles at 21 days. The experiment was performed as in Figure 3, except that the mice were sacrificed 21 days after the oropharyngeal aspiration. BALF was collected to determine the TGF-β1 (A) level. (B) The total collagen content of the lung tissues was determined by the Sircol collagen kit (Biocolor Ltd., Carrickfergus, U.K.). QTZ at 5.0 mg/kg was treated as positive control. \*  $p < 0.05$  compared to control.

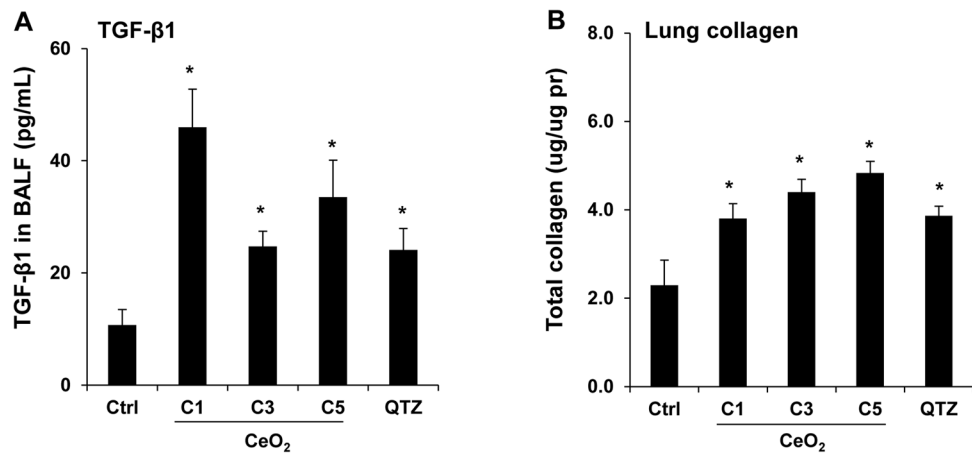
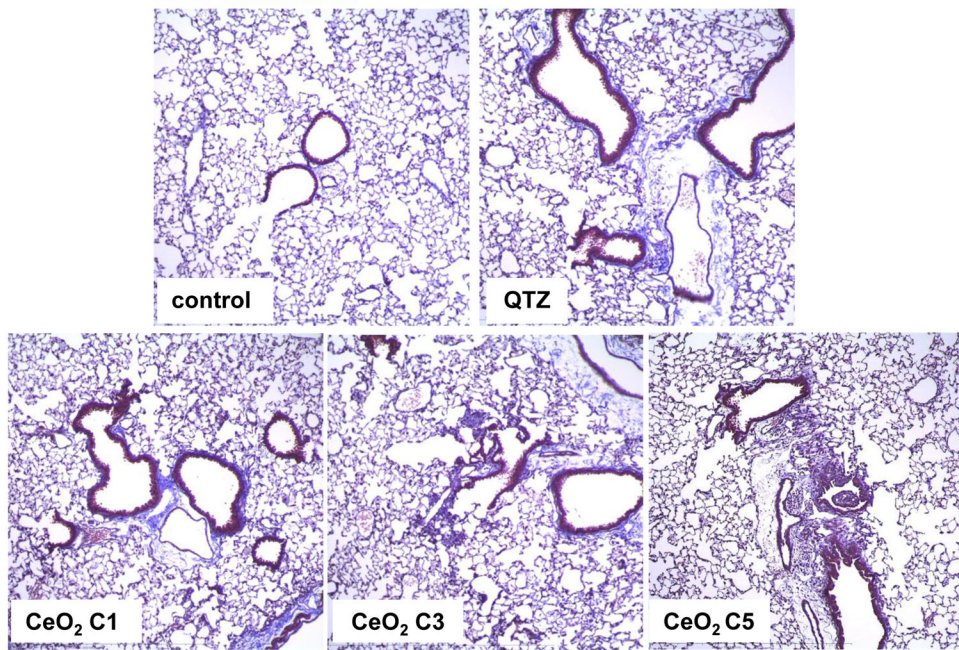
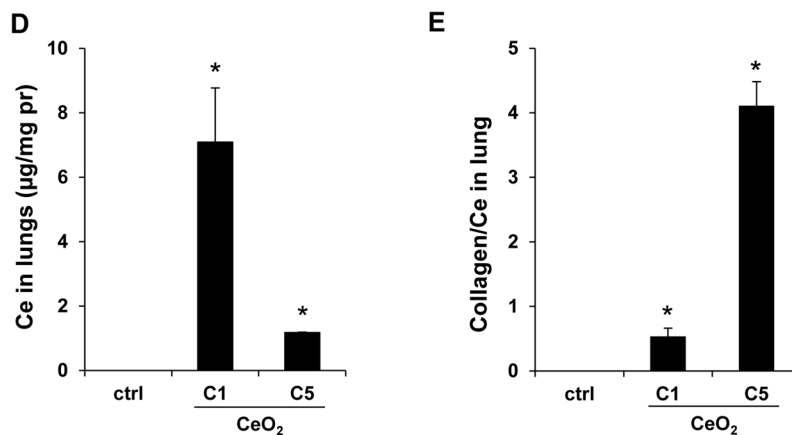


Figure 5C

44 d **Trichrome**



**Figure 5.**

Sub-chronic pulmonary effects of CeO<sub>2</sub> nanoparticles at 44 days. (A) TGF-β1 levels in BALF and (B) total collagen content of the lungs of mice receiving 4 mg/Kg CeO<sub>2</sub> nanoparticles. The animals were sacrificed after 44 days and all lung tissues were collected to determine the total collagen as described in Figure 4. (C) Lung sectioning and staining with Masson's trichrome. Areas of concentrated blue staining represents collagen deposition sites. QTZ at 5.0 mg/kg served as positive control. (D) ICP-OES analysis to determine elemental Ce content in the lungs of mice receiving the same dose of C1 and C5 nanoparticles, followed by sacrifice after 44 days. (E) Comparative analysis of the collagen content in the lung of C1 and C5 exposed mice after correction for Ce content. This was accomplished by normalizing the total collagen content to the total elemental Ce content and expressed as collagen/Ce in lung. \*  $p < 0.05$  compared to control.



Figure 6A

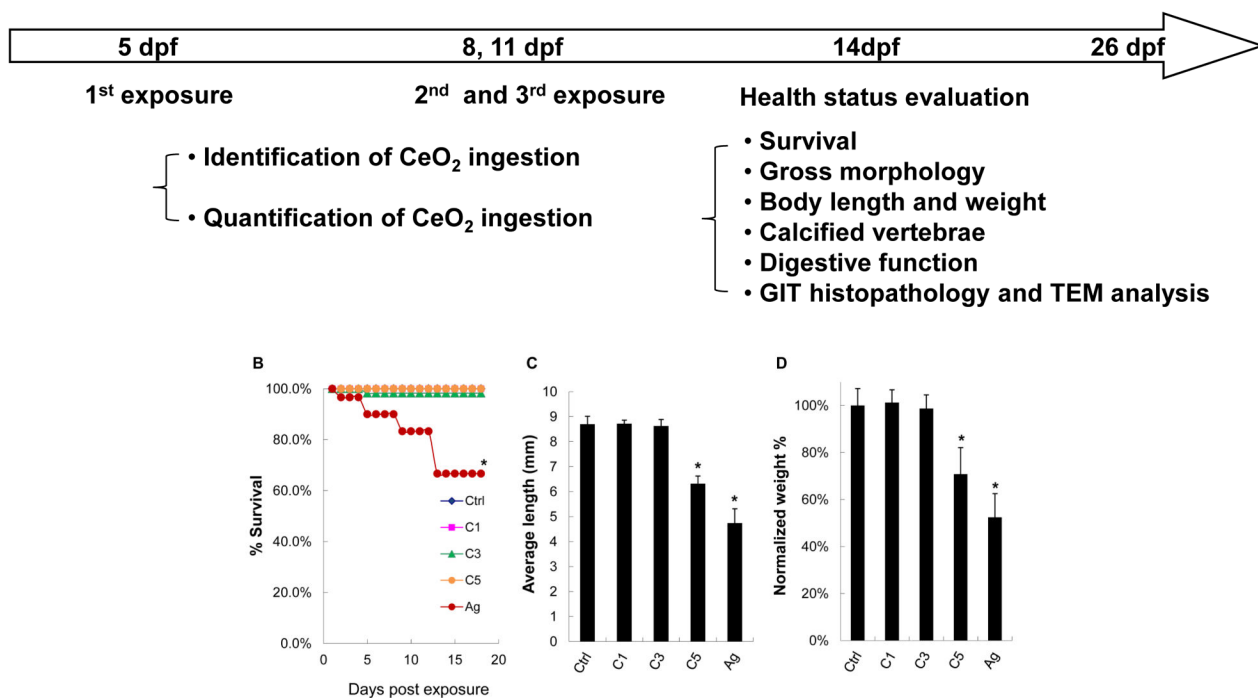
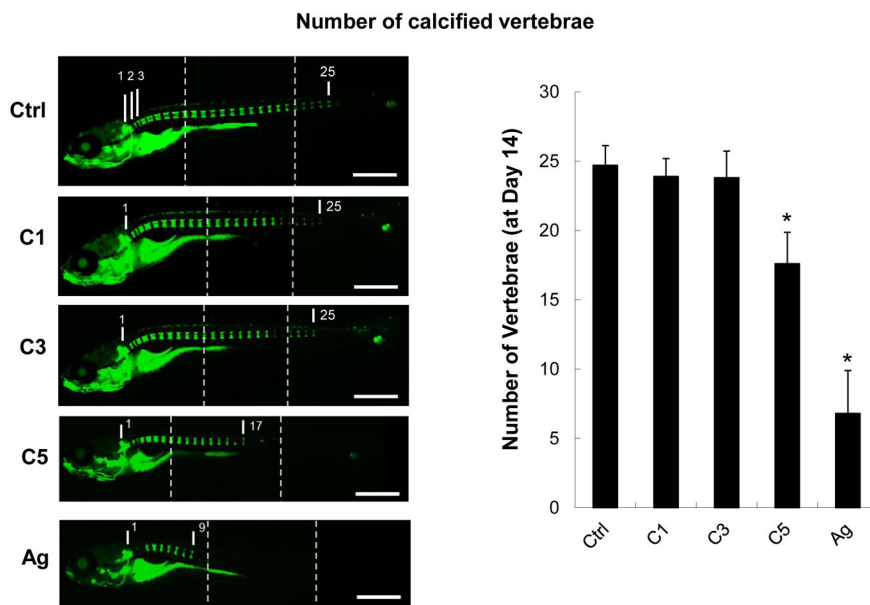


Figure 6E



**Figure 6.** Pulse-exposure of zebrafish larvae to CeO<sub>2</sub> nanoparticles to assess the effect of AR on larval development. (A) Diagram showing the stepwise pulse-exposure protocol. Zebrafish larvae

at 5 dpf were incubated in CeO<sub>2</sub> nanoparticle suspensions in petri dishes. Thirty larvae were exposed on each occasion to 25 µg/mL nanoparticles for 6 hr. The larvae were carefully and thoroughly washed before returning to standard aquarium tanks for regular feeding and water circulation. The same batch of larvae was used for secondary and tertiary exposures at 8 and 11 dpf. The survival rate of larvae was monitored daily and the overall health status of the larvae assessed on 14 dpf based on morphology features, body length and weight, number of calcified vertebrae and digestive function. Larvae were also randomly selected for histology and TEM analyses. (B) The survival rate of untreated larvae or larvae exposed to C1, C3, C5 and AgNPs. Only the larvae exposed to AgNPs (positive control) showed decreased survival. (C) Average larval length at 14 dpf. Larvae exposed to C5 and AgNPs showed significantly reduced length. (D) Average larval weight showed that C5 and AgNPs exposures resulted in significantly lower body weight. (E) Use of the number of calcified vertebrae as assessed by calcein staining. The representative fluorescence images show that control or larvae exposed to C1 and C3 exhibit 25 calcified vertebrae at 14 dpf. By contrast, larvae exposed to C5 and AgNPs showed ~17 and ~9 calcified vertebrae, respectively. Three images were captured and blended to cover the total body length, as indicated by the dashed line s. \* p < 0.05 compared to control. Scale bar: 1 mm.

Figure 7A

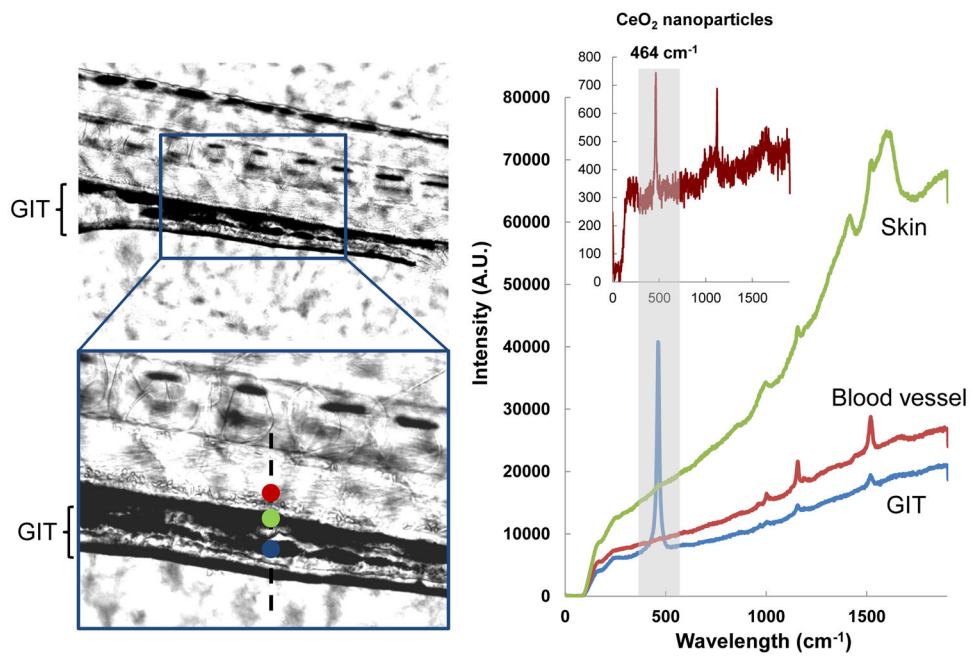
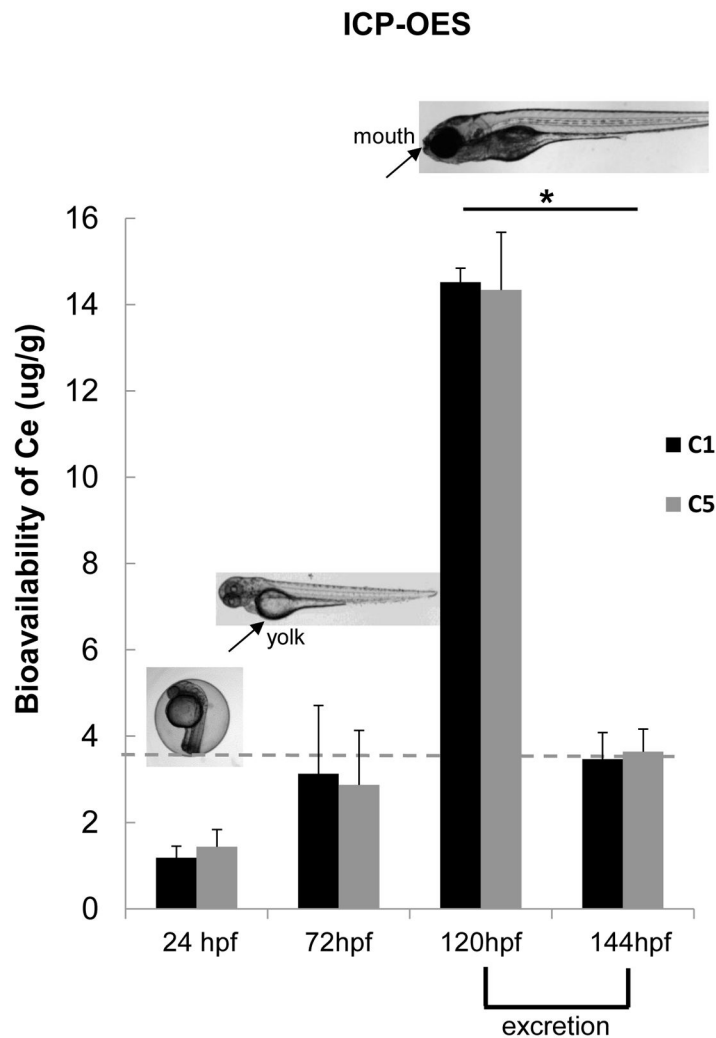
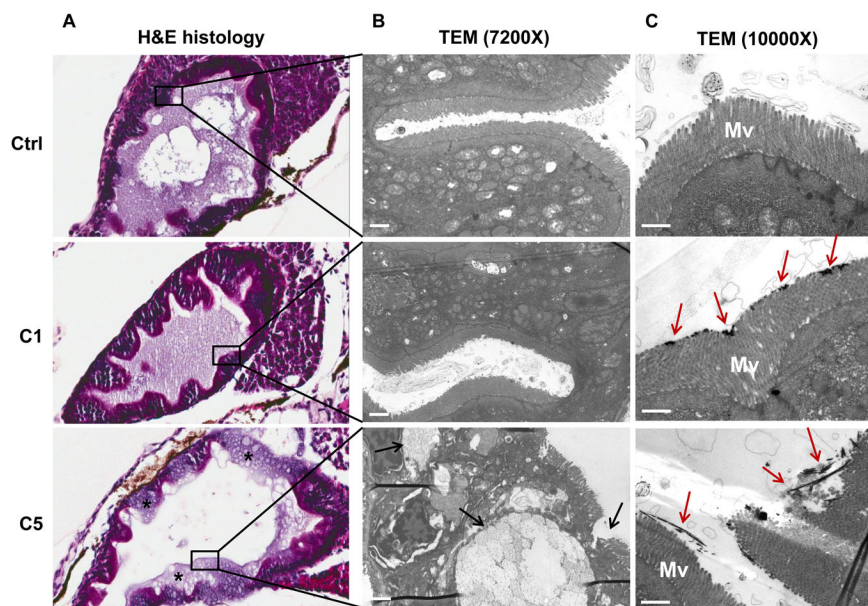


Figure 7B

**Figure 7.**

Confocal-Raman microscopy and ICP-OES analyses of  $\text{CeO}_2$  uptake in zebrafish embryos and larvae after nanoparticle exposure. (A) Confocal Raman microscopy analysis was conducted on the C5 exposed larvae. The signature Raman scattering peak of  $\text{CeO}_2$  (centered at  $464\text{ cm}^{-1}$ ) confirmed the presence of C5 inside the GIT. Raman spectra collected from the skin (green dot) or the blood vessels (red dot) did not show any signature peak for  $\text{CeO}_2$ . Developing larvae were anesthetized and placed on a glass slide with concavity wells. The excitation laser beam (514 nm) was programmed to scan across the lateral view of developing larvae as indicated by the dashed line. Raman scattering spectra were collected across this line at three spots (red dot = skin, green = blood vessel, blue = GIT). Among these, only the blue spot showed a Raman signature similar to that of  $\text{CeO}_2$  nanoparticles (provided in the insert). (B) Groups ( $n = 50$ ) of embryos (24 and 72 hpf) and larvae (120 hpf) were incubated with  $25\text{ }\mu\text{g/mL}$   $\text{CeO}_2$  (C1 and C5) for 6 hr. The embryos and larvae were thoroughly washed before acid digestion and assessment of the amount ( $\mu\text{g}$ ) of Ce by ICP-OES. The elemental Ce content in 24 and 72 hpf embryos were 1.5–3.0  $\mu\text{g/g}$

of embryos, which is close to the detection limit of ICP-OES (indicated in grey dash line). This quantity went up to 14.52 and 14.34  $\mu\text{g/g}$  of larvae exposed to C1 and C5 respectively if the exposure was performed at 120 hpf. However, incubation of these larvae for an additional 24 hr (*i.e.*, up to 144 hpf) showed a significant reduction in the Ce content upon elimination from the gut (\*  $p < 0.05$ ). There was no statistical significant difference between uptake of C1 and C5 in any time point.



**Figure 8.** Histological and TEM analysis of the GIT. (A) Histopathology analysis shows the structural damage by C5 (but not C1) to the GIT. C5 exposed larvae showed desquamation of enterocytes and damage to the epithelial lining (marked by \*). The control larvae and C1 exposed larvae showed normal enterocyte histology and an intact lining. (B) TEM analysis of a thin GIT section reveals ultrastructural damage by C5. This included blunting or loss of microvilli (marked by black arrows). (C) TEM analysis of the GIT immediately following CeO<sub>2</sub> exposure for 6 hr. While C1 agglomerates could be seen to loosely adhere to the tips of the microvilli, C5 bundles could be seen to pierce through the microvilli, disrupting their integrity (marked by red arrows). Mv= microvilli. Scale bar: 1  $\mu$ m.

Figure 9A.

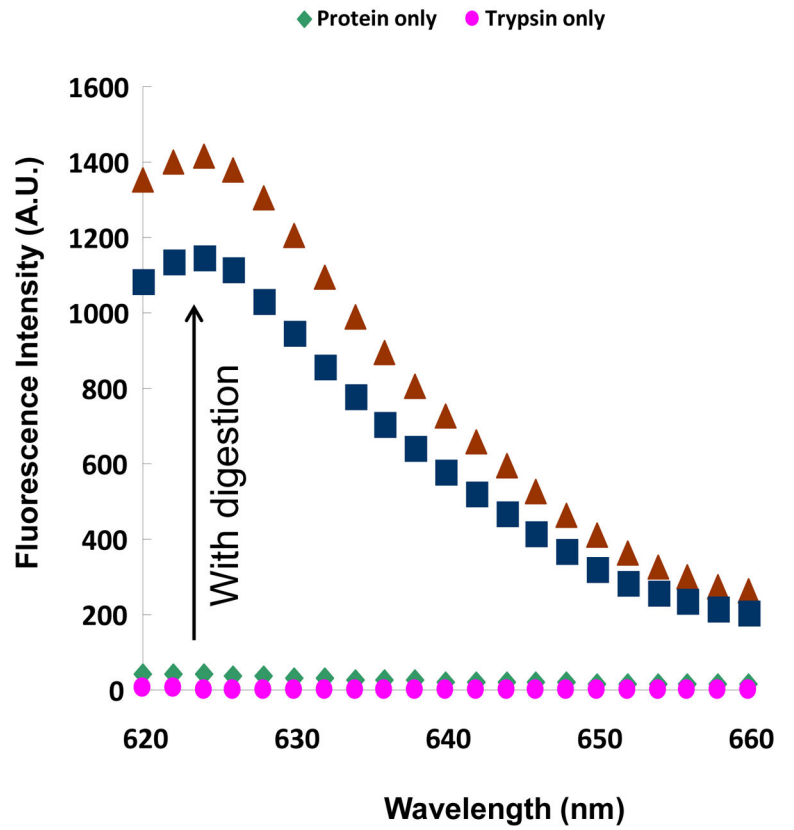
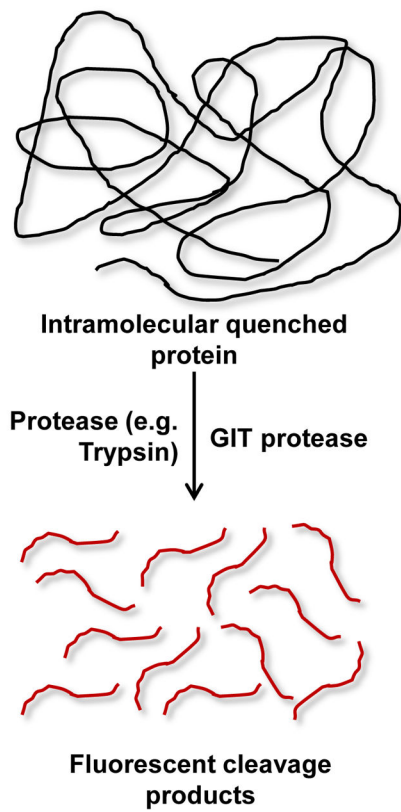
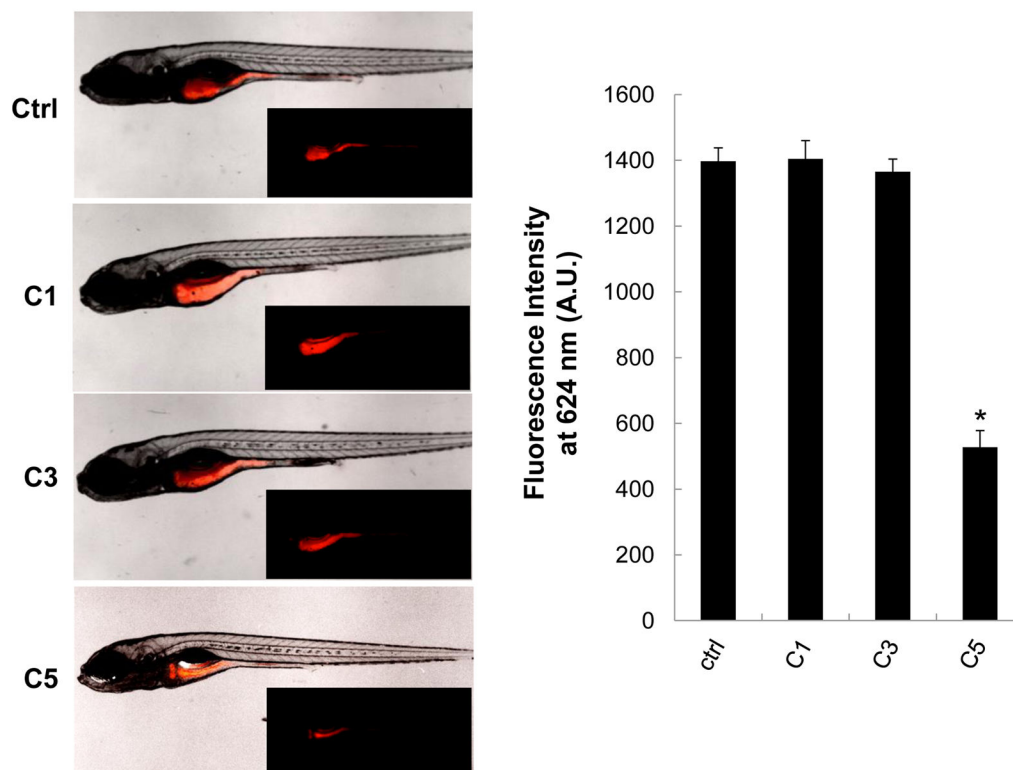


Figure 9B

**Figure 9.**

The digestive function of larvae exposed to C5 was significantly reduced compared to control or C1/C3 exposed larvae. (A) Explanation of the principle of digestive function testing. Quantification of the fluorescence intensity of the intramolecular-quenched protein, EnzChek, at 624 nm following experimental digestion by trypsin. (B) Left panel: representative fluorescent images of larvae fed with EnzChek. The fluorescence intensity of the digested peptides in the GIT of larvae exposed to C5 is significantly reduced compared to the fluorescence intensity in larvae exposed to C1 and C3. Right: Average  $\pm$  SD of the fluorescence intensity extracted from larvae in each group. While fluorescence intensity was significant ( $p < 0.05$ ) reduced for C5 exposed larvae, no decrease was seen for C1 and C3 exposed larvae.